Evaluating the Tm2+ 4f125d1 → 4f13 and 4f13 → 4f13 Luminescence and Quenching Dynamics in Orthorhombic BaCl2

Plokker, M.P.; Vlaar, S.A.; Bakx, A.H.J.; van der Kolk, E.; Dorenbos, P.; Hintzen, H.T.J.M.

DOI
10.1021/acs.jpcc.3c04638

Publication date
2023

Document Version
Final published version

Published in
The Journal of Physical Chemistry C

THE JOURNAL OF PHYSICAL CHEMISTRY C
A JOURNAL OF THE AMERICAN CHEMICAL SOCIETY

pubs.acs.org/JPCC
Article

Evaluating the Tm^{2+} $4f^{12}5d^1 \rightarrow 4f^{13}$ and $4f^{13} \rightarrow 4f^{13}$ Luminescence and Quenching Dynamics in Orthorhombic $BaCl_2$

Maarten P. Plokker,* Sophie Vlaar, Aaron H. J. Bakx, Erik van der Kolk, Pieter Dorenbos, and Hubertus T. Hintzen

Cite This: J. Phys. Chem. C 2023, 127, 19017−19026

ABSTRACT: The luminescence properties of Tm^{2+}-doped $BaCl_2$ with an orthorhombic structure have been studied as a function of temperature and compared to other Tm^{2+}-doped chlorides. In addition to the $^2F_{5/2} \rightarrow {}^2F_{7/2}$ ($4f^{13} \rightarrow 4f^{13}$) line emission, two $4f^{12}5d^1 \rightarrow 4f^{13}$ band emissions are observed at 20 K that can be ascribed to the spin-allowed $(^3H_6,5d^1)_{S=1/2} \rightarrow {}^2F_{7/2}$ and spin-forbidden $(^3H_6,5d^1)_{S=3/2} \rightarrow {}^2F_{7/2}$ transitions. So far, the Tm^{2+} spin-allowed $(^3H_6,5d^1)_{S=1/2} \rightarrow {}^2F_{7/2}$ transition has only been identified in Tm^{2+}-doped iodides and some bromides but never before in a Tm^{2+}-doped chloride. Its presence in orthorhombic $BaCl_2:Tm^{2+}$ is explained by the absence of a $(^3H_6,5d^1)_{S=1/2} \rightarrow (^3H_6,5d^1)_{S=3/2}$ energy transfer process. As the temperature increases, both $4f^{12}5d^1 \rightarrow 4f^{13}$ emissions undergo rapid quenching and are no longer observed at 120 K, resulting in an intensity increase of the $4f^{13} \rightarrow 4f^{13}$ emission. However, above 100 K, the intensity of the $4f^{13} \rightarrow 4f^{13}$ emission also decreases, most likely due to quenching via $(^3H_6,5d^1)_{S=3/2} \rightarrow {}^2F_{7/2}$ interband crossing, as enabled by the exceptionally large $4f^{12}5d^1$ Stokes shift.

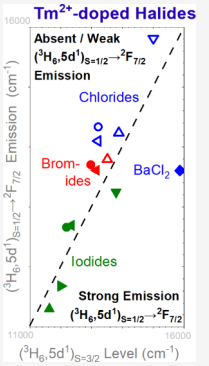

1. INTRODUCTION

Over the past years, various Tm^{2+}-doped halide systems have been investigated and used for different applications. During the 1960s, $AF_2:Tm^{2+}$ (A = Ca, Ba, and Sr) halides were intensely studied for use in solid-state rare earth-based masers.[1−4] These materials were synthesized via the Bridgman−Stockbarger method,[5] using AF_2 and TmF_3 starting compounds, after which the Tm^{3+} valency was reduced to Tm^{2+} by X-ray irradiation.[6,7] However, due to A^{2+} and Tm^{3+} charge compensation issues during the synthesis, this research was eventually abandoned.[4]

Years later, in 1994, Schipper et al.[8] investigated the suitability of SrB_4O_7 as a host for divalent lanthanide doping and made the very first observation of a Tm^{2+} $4f^{12}5d^1 \rightarrow 4f^{13}$ emission. These materials are currently still studied for the interest of luminescence thermometry and manometry.[9,10] However, for the Tm^{2+}-doped halides, it was not until the late 90s that advances in synthesis techniques and charge reduction methods[11−13] were significantly exploited. In 2000, Wickleder[14] investigated the $4f^{12}5d^1 \rightarrow 4f^{13}$ emissions of Tm^{2+} in $SrZnCl_4$ and $BaZnCl_4$ halides. A year later, Wickleder and researchers from Bern University successfully demonstrated the process of upconversion in $SrCl_2:Tm^{2+}$.[15] This triggered a fierce quest for more Tm^{2+}-doped halides, in which this rare phenomenon could be observed. At the time, Grimm and Beurer from Bern University studied the Tm^{2+} $4f^{12}5d^1 \rightarrow 4f^{13}$ and $4f^{13} \rightarrow 4f^{13}$ temperature-dependent luminescence in predominantly $CsCaX_3$ (X = Cl, Br, and I), $RbCaI_3:Tm^{2+}$, and ACl_2 (A = Ca, Sr, and Ba) halides, obtaining valuable information on the $4f^{12}5d^1$-$4f^{13}$ quenching dynamics.[16−22] A decade later, in 2015, ten Kate et al.[23] discovered the potential suitability of Tm^{2+}-doped halides for luminescence solar concentrators. In the wake of this discovery, we reinvestigated the Tm^{2+} thermal quenching dynamics and studied it in several host lattices, such as NaX, CaX_2 (X = Cl, Br, and I), and SrI_2, and in addition, in halide solid solutions of $CsCa(Cl/Br)_3$ and $CsCa(Br/I)_3$.[24−27] In view of these recent results, the previous study of Grimm et al.[21] on $BaCl_2:Tm^{2+}$ with an orthorhombic structure raises several open questions. First, the existence of two $4f^{12}5d^1 \rightarrow 4f^{13}$ emissions from the $(^3H_6,5d^1)_{S=3/2}$ state is reported. To our knowledge, this has not been observed before in the literature for other chloride host lattices with only a single cation site. Second, these two emissions were proposed to quench via multiphonon relaxation. In the case of $BaCl_2:Sm^{2+}$, with an orthorhombic structure, the early work of Lauer and Fong[28] supports a quenching of the Sm^{2+} $4f^55d^1 \rightarrow 4f^6$ emission via multiphonon relaxation. However, later works by He et al.[29] and Dixie et al.[30] on $BaCl_2:Sm^{2+}$ suggest the claim of quenching via interband crossing. Embroidering on our numerical work for $CaX_2:Tm^{2+}$ (X = Cl, Br, and I) where the $4f^{12}5d^1 \rightarrow 4f^{13}$ emissions were found to quench via multiphonon relaxation and interband crossing, we zoom in on the two $4f^{12}5d^1 \rightarrow 4f^{13}$ emissions of $BaCl_2:Tm^{2+}$, with an

Received: July 10, 2023
Revised: August 30, 2023
Published: September 13, 2023

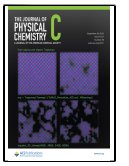

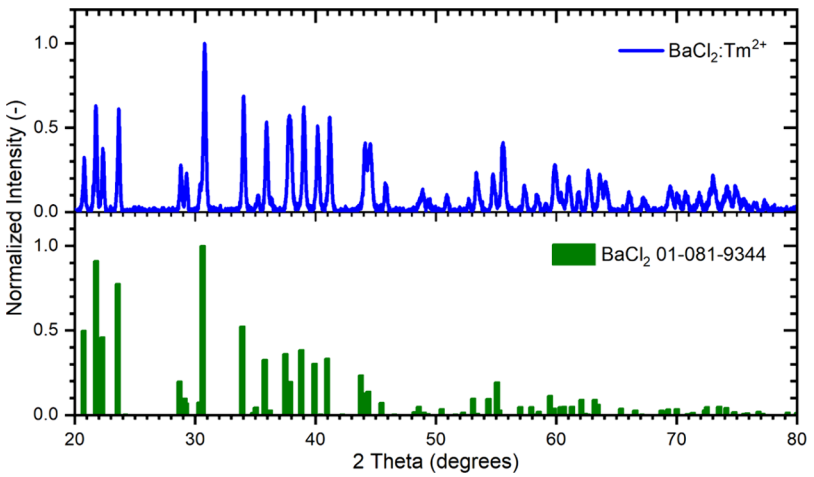

Figure 1. Normalized powder X-ray diffraction pattern of the $BaCl_2$:Tm^{2+} sample at room temperature. The pattern matches the reference pattern of orthorhombic $BaCl_2$[35] with a cotunnite $PbCl_2$ structure and the space group *Pnma* (no. 62).

orthorhombic structure, in an attempt to shed new light on their quenching via a qualitative analysis.

2. METHODS

2.1. Sample Synthesis. The $BaCl_2$:Tm^{2+} powder sample was prepared by mixing $BaCl_2$ (Sigma-Aldrich, 99.9%) with 1 mol % TmI_2. The mixture was ground into a homogeneous powder, transferred into a quartz ampule, and subsequently attached to a vacuum/inert gas system. After evacuation to 10^{-1} mbar, the system was purged three times with dry nitrogen. The ampule was then evacuated further to 10^{-3} mbar, and the powder was heated for 2−2.5 min using four Tecla burners. Upon liquification of the powder, the heating was stopped. The solidified sample was then removed from the ampule and ground into a fine powder. All handlings were performed under strictly inert and dry conditions in a glovebox (MBraun, Garching, Germany).

2.2. Characterization Measurements. The X-ray diffraction (XRD) pattern of the powder sample was obtained with a Philips X'pert-Pro diffractometer (Philips, Eindhoven, The Netherlands) in Bragg−Bretano geometry using CuKα radiation. The measurement took place at room temperature from 10° to 80° 2θ with a 0.008° resolution. In addition, the Tm concentration in the sample was determined via inductively coupled plasma−optically enhanced spectroscopy (ICP-OES) measurements using a PerkinElmer Optima 4300DV spectrometer (PerkinElmer, Waltham, Massachusetts, USA). Diluted standards of Tm and Ba with known concentrations were used to constitute an intensity-concentration calibration line. The diffuse reflectance spectra were acquired with a Bruker Vertex V80 spectrometer (Bruker, Karlsruhe, Germany). The determined Tm^{2+} $4f^{13} \rightarrow 4f^{13}$ and Tm^{3+} $4f^{12} \rightarrow 4f^{12}$ Kubelka−Munk absorptions were used to estimate the Tm^{2+}/Tm^{3+} ratio present in the sample. Fluorescence quantum yield measurements were performed using an Edinburgh FLS980 spectrometer (Edinburgh Instruments, Livingston, UK) with an integrating sphere, a 450 W xenon arc lamp, and a Hamamatsu C9940-02 near-infrared (NIR) PhotoMultiplier Tube (PMT) (Hamamatsu Photonics, Hamamatsu, Japan).

2.3. Temperature-Dependent Optical Measurements. The temperature-dependent excitation and emission spectra were obtained with the help of a xenon lamp coupled to a double monochromator with three gratings and a R7600U-20HV-800 V PMT, H1033A-75 NIR-PMT, or C9100-13 EM-CCD (all Hamamatsu Photonics, Hamamatsu, Japan) that was in turn attached to a single monochromator with three gratings. A calibrated EPLAB NBS 1000W Quartz Iodine lamp was used to acquire the wavelength-dependent sensitivity of the detectors. The detection ranges of 400:1150 and 950:1600 nm for CCD and NIR-PMT, respectively, share an overlap that allows for a connection of the output of both detectors and hence accurately determine the Tm^{2+} $4f^{12}5d^1 \rightarrow 4f^{13}$ and $4f^{13} \rightarrow 4f^{13}$ emission intensity ratios over temperature. Therefore, a small spatula amount of $Ca_2Si_5N_8$:Yb^{3+} was added to the samples. After Yb^{3+} was excited at 360 nm, the $^2F_{5/2} \rightarrow {}^2F_{7/2}$ emission at 985 nm was observed and used for the detector coupling.

The samples were heated and cooled by an APD Cryogenic Helium cooler (APD Cryogenics, Allentown Pennsylvania, USA) and a Lakeshore temperature controller (Lakeshore Cryotronics, Westerville Ohio, USA). Special sample holders were used for all measurements to prevent unwanted hygroscopic and oxidation reactions.[31]

3. RESULTS AND DISCUSSION

3.1. Sample Characterization. Anhydrous $BaCl_2$ exists in two temperature-dependent structural modifications. At high temperatures, the β-form that carries the cubic NaCl rock-salt structure with the space group *Fm*3*m* (no. 225) is likely to form, whereas at low temperatures, the α-form with the orthorhombic cotunnite $PbCl_2$ structure and the space group *Pnma* (no. 62) arises. In contrast to the β-form, the α-form is the thermodynamically stable modification at room temperature.[28,32−34] Figure 1 shows the XRD pattern of our $BaCl_2$:Tm^{2+} sample, which matches with the reference pattern of the α-form.[35] Only a single Ba^{2+}-site is present in this orthorhombic structure, exhibiting C_S point group site symmetry with a 9-fold anion coordination geometry, which is represented in shape by the distorted tricapped trigonal prism displayed in Figure 2. The ionic radius of the Ba^{2+} cation for 9-fold coordination (1.47 pm[36]) is much larger than that of Tm^{2+} (estimated value: 1.2 pm[36]). For Tm^{2+} substituted on the Ba^{2+}-site, the long Tm^{2+}−Cl^- distances for 9-fold coordinated Tm^{2+} on an asymmetric site result in a weak crystal field. The strong deviation in the ionic radius is likely to

https://doi.org/10.1021/acs.jpcc.3c04638
J. Phys. Chem. C 2023, 127, 19017−19026

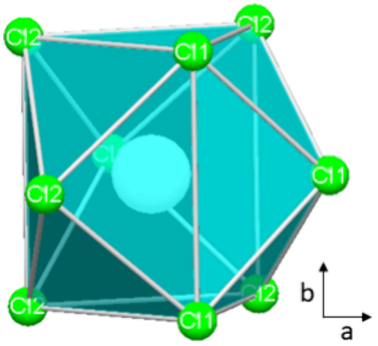

Figure 2. Graphical representation of the distorted tricapped trigonal prism related to the 9-fold coordination geometry around Tm^{2+} when this ion is present in $BaCl_2$ with an orthorhombic structure.

lead to local distortions and defects, as Tm^{2+} occupies the Ba^{2+}-sites. This would be bolstered by the presence of Tm^{3+} in the sample, for which charge compensation is required when it is incorporated on the Ba^{2+}-site.

Figure 3 shows the Kubelka–Munk (K–M) absorption spectrum. In this spectrum, the Tm^{2+} absorption peaks are indicated in green, and the ones related to Tm^{3+} are marked in red. Throughout this work, we will use the short-hand notation $^{2S+1}L_J$ to assign the Tm^{3+} $4f^{12}$ and Tm^{2+} $4f^{13}$ levels and $(^{2S+1}L_J,5d^1)S$ to refer to the excited Tm^{2+} $4f^{12}5d^1$ levels. For this latter notation, $^{2S+1}L_J$ represents the state of $4f^{12}$ and S denotes the combined $4f^{12}$ and $5d^1$ electron spin of the excited state.

The K–M absorption spectrum displays the characteristic $Tm^{3+3}H_6 \rightarrow {}^3F_{2,3}$, $^3H_6 \rightarrow {}^3H_4$, and $^3H_6 \rightarrow {}^3H_5$ line absorptions. These $4f^{12} \rightarrow 4f^{12}$ absorptions are respectively positioned near 700, 800, and 1230 nm, which is in close analogy to the Dieke diagram.[37] In addition, the onset of a broad absorption band is observed close to 600 nm. This band is likely to represent the $Tm^{2+2}F_{7/2} \rightarrow (^3H_6,5d^1)_{S=1/2}$ transition, which appears most intense due to its $4f^{13} \rightarrow 4f^{12}5d^1$ parity-allowed nature, as explained in more detail in Section 3.2. Furthermore, a sharp and weak absorption peak is seen near 1140 nm. This peak portrays the $Tm^{2+2}F_{7/2} \rightarrow {}^2F_{5/2}$ parity-forbidden $4f^{13} \rightarrow 4f^{13}$ absorption, which has been observed by us several times before for Tm^{2+}-doped NaX and CaX_2 (X = Cl, Br, and I).[24,26] In one of these studies,[24] diffuse reflectance measurements were performed on NaI samples doped with purely Tm^{2+} or Tm^{3+}. From the computed Kubelka–Munk absorption spectra, the intensities of the $Tm^{2+2}F_{7/2} \rightarrow {}^2F_{5/2}$ and $Tm^{3+3}H_6 \rightarrow {}^3H_5$ absorption bands were separately integrated and compared to the absolute Tm (i.e., Tm^{2+} or Tm^{3+}) concentrations from ICP-OES measurements. This enabled us to determine the relative Tm^{2+} and Tm^{3+} absorption strengths in NaI to be 1 versus 3.4. Upon applying this factor to the integrated $Tm^{2+2}F_{7/2} \rightarrow {}^2F_{5/2}$ and $Tm^{3+3}H_6 \rightarrow {}^3H_5$ absorption intensities, the Tm^{2+}/Tm^{3+} ratio in the BaCl:Tm sample synthesized in this study is estimated to be 3/8.

From the ICP-OES measurement, the absolute Tm concentration in the sample was determined at 1.1 ± 0.1 mol %. This value is in close agreement with the doping percentage calculated from the weighted amount of TmI_2 as reported in Section 2.1 and listed for convenience in Table 1. Upon multiplying the estimated Tm^{2+}/Tm^{3+} ratio with the absolute Tm concentration, the Tm^{2+}-doping concentration in the sample amounts to approximately 0.3 mol %.

Table 1. Summary Overview of the Sample Characterization Measurements

sample	structure	mol % TmI_2[a]	mol % Tm[b]	Tm^{2+}/Tm^{3+} ratio[c]	mol % Tm^{2+}[d]	Tm^{2+} QY (%)[e]
$BaCl_2:Tm^{2+}$	$PbCl_2$	1.0	1.1	3/8	0.3	19 ± 1

[a]Nominal doping. [b]ICP-OES. [c]K–M absorption spectra. [d]Calculated from ICP-OES and K–M absorption spectra. [e]λ_{exc} = 570 nm {Tm^{2+} $(^3H_6,5d^1)_{S=1/2}$ band}.

As a final step in the characterization, room-temperature quantum yield measurements were performed on the $BaCl_2:Tm^{2+}$ sample after photoexcitation at 570 nm into the Tm^{2+} $(^3H_6,5d^1)_{S=1/2}$ band. To correct for the absorption contribution by the host, an identical measurement was executed on pure unheated orthorhombic $BaCl_2$. This value was estimated at 9.9 ± 0.5%, so the host-corrected absorption (i.e., absorption due to Tm^{2+}) amounted to 16 ± 0.8%. The quantum efficiency (QE) of the $Tm^{2+2}F_{5/2} \rightarrow {}^2F_{7/2}$ ($4f^{13} \rightarrow 4f^{13}$) emission was then established to be 19 ± 1%. This value is in close order to that of NaCl:Tm^{2+} and $CaCl_2:Tm^{2+}$ and indicates a large loss contribution at room temperature by a

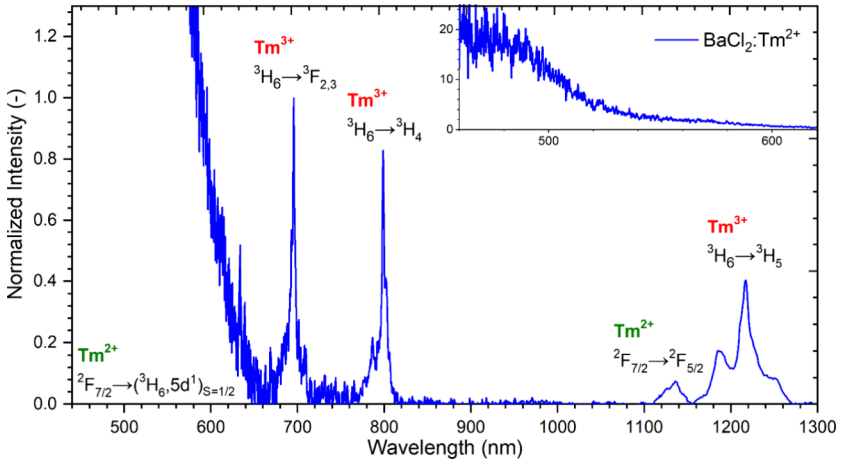

Figure 3. Kubelka–Munk (K–M) absorption spectrum of the $BaCl_2:Tm^{2+}$ sample as normalized on the $Tm^{3+3}H_6 \rightarrow {}^2F_{2,3}$ absorption. The related Tm^{2+} absorptions are labeled by their transition in green, while the Tm^{3+} absorption peaks are indicated in red.

https://doi.org/10.1021/acs.jpcc.3c04638
J. Phys. Chem. C 2023, 127, 19017–19026

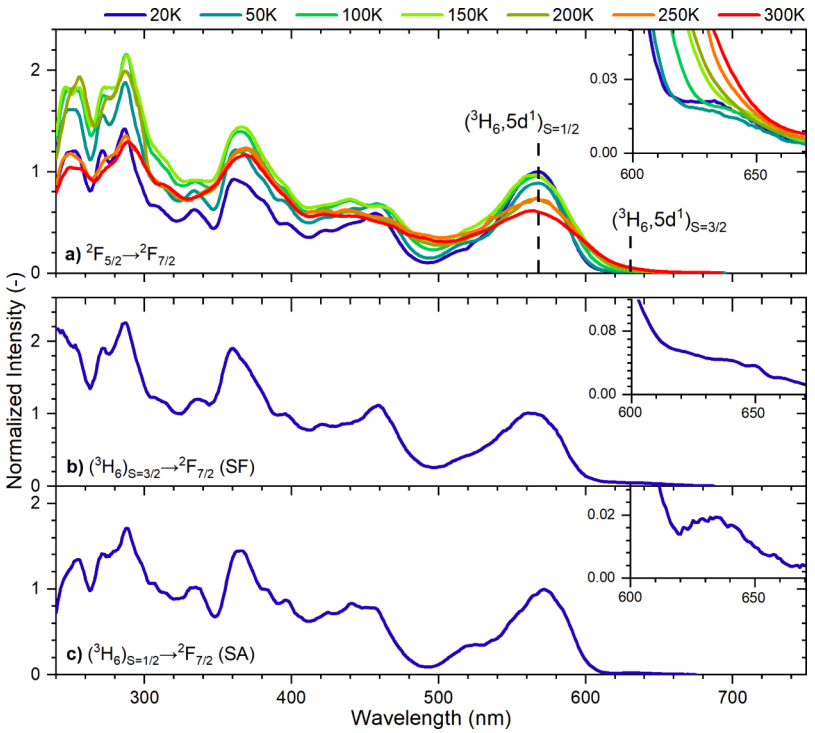

Figure 4. Normalized Tm^{2+} excitation spectra of the $^2F_{5/2} \rightarrow {}^2F_{7/2}$ emission at 1140 nm (a) as displayed over a broad temperature range. The low-spin $(^3H_6,5d^1)_{S=1/2}$ levels are indicated in the main figures, while the insets focus on the high-spin $(^3H_6,5d^1)_{S=3/2}$ levels. Panels (b) and (c) respectively display the 20 K excitation spectra as obtained on the spin-forbidden $(^3H_6,5d^1)_{S=3/2} \rightarrow {}^2F_{7/2}$ emission at 815 nm and spin-allowed $(^3H_6,5d^1)_{S=1/2} \rightarrow {}^2F_{7/2}$ emission at 735 nm. The identification of these two emissions is discussed in the subsequent subsection.

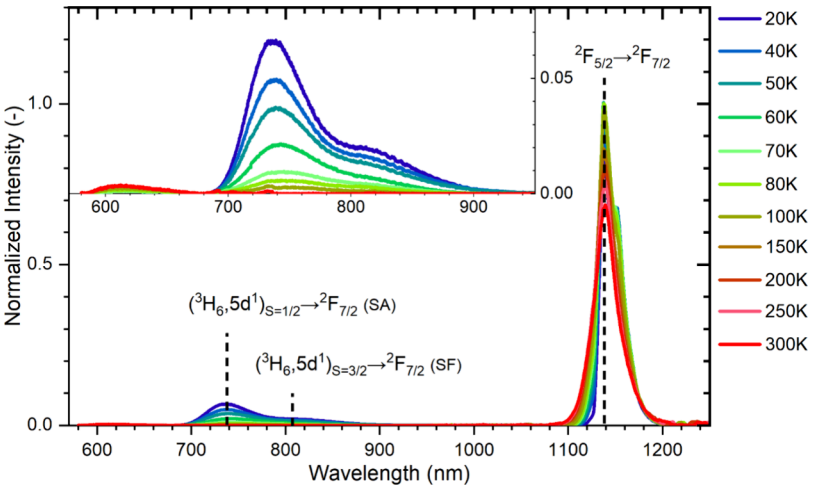

Figure 5. Normalized emission spectra of Tm^{2+} as a dopant in orthorhombic $BaCl_2$ at different temperatures and normalized on the $^2F_{5/2} \rightarrow {}^2F_{7/2}$ ($4f^{13} \rightarrow 4f^{13}$) emission at 20 K. Photoexcitation occurred within the $(^3H_6,5d^1)_{S=1/2}$ levels at 570 nm. The inset shows a close-up of the $4f^{12}5d^1 \rightarrow 4f^{13}$ emissions, where the spin-allowed $(^3H_6,5d^1)_{S=1/2} \rightarrow {}^2F_{7/2}$ emission is much more intense than the spin-forbidden $(^3H_6,5d^1)_{S=3/2} \rightarrow {}^2F_{7/2}$ emission. A small feature possibly related to weak defect emission or an artifact of the sample holder is observed at 615 nm. The emission spectra are corrected for the sensitivity of detection via the method described in Section 2.3.

possible radiationless quenching route going (in)directly from the $(^3H_6,5d^1)_{S=1/2}$ levels to the $^2F_{7/2}$ ground state.[24,26]

3.2. Tm^{2+} Luminescence and Quenching Dynamics.

As a next step, the Tm^{2+} quenching dynamics in orthorhombic $BaCl_2$ were qualitatively investigated. Since both Tm^{2+} and Tm^{3+} are present in the sample, the Tm^{2+} ions were selectively excited at a monochromic wavelength where there are no nearby Tm^{3+} levels and, hence, no Tm^{3+} ions are excited.[37] At first, the temperature-dependent excitation spectra are made on the $Tm^{2+}{}^2F_{5/2} \rightarrow {}^2F_{7/2}$ emission, from which the lowest energy excitation bands are classified. Next, the temperature-dependent emission spectra are presented and the observed emissions are identified and labeled to their electronic transition. Finally, the intensity of the different emissions is monitored over a broad temperature range, allowing for a qualitative interpretation of the luminescence and quenching.

3.2.1. Assignment of Excitation Bands. Figure 4a shows the excitation spectra as acquired from the $Tm^{2+}{}^2F_{5/2} \rightarrow {}^2F_{7/2}$ ($4f^{12} \rightarrow 4f^{12}$) emission at various temperatures. The shape of these spectra closely resembles the 11 K absorption spectra of

https://doi.org/10.1021/acs.jpcc.3c04638
J. Phys. Chem. C 2023, 127, 19017−19026

$BaCl_2$:Tm^{2+}, with an orthorhombic structure, as reported previously by Grimm et al.[21] For Tm^{2+} as a dopant in orthorhombic $BaCl_2$, the $4f^{12}5d^1$ levels are split several times by different interactions. The crystal field interaction with C_s symmetry splits the $4f^{12}5d^1$ level into five nondegenerate $4f^{12}5d^1$ sublevels. In addition, the Coulomb repulsion and spin−orbit coupling within the $4f^{12}$-configuration lead to a further splitting of each Tm^{2+} $4f^{12}5d^1$ level into $^{2S+1}L_J$ terms that are analogous to the Tm^{3+} multiplets in the Dieke diagram. On top of that, the exchange interaction between the spin of 5d- and 4f-electrons results in an additional splitting into low-spin (LS) $S = 1/2$ and high-spin (HS) $S = 3/2$ states. Due to the very small crystal field splitting, no clear separation can be made between the different $4f^{12}5d^1$ levels and, therefore, only the lowest energy $4f^{12}5d^1$ sublevels can be identified.[16,38−41]

In the work of Brixner and Ferretti,[32] on orthorhombic $BaCl_2$:Eu^{2+}, the lowest energy Eu^{2+} $4f^65d^1$ excitation level is located at 375 nm or 26670 cm^{-1}. When adding this energy value to the energy difference between the lowest LS $4f^{12}5d^1$ and $4f^65d^1$ levels of free Tm^{2+} and Eu^{2+},[41] respectively, the Tm^{2+} $(^3H_6,5d^1)_{S=1/2}$ LS excitation band should be located at around 17545 cm^{-1} or 560 nm. The excitation spectra in Figure 4a indeed show a broad excitation band located close to 570 nm that can hence be classified as the Tm^{2+} $(^3H_6,5d^1)_{S=1/2}$ LS excitation levels. In addition, the energy difference between the $4f^{12}5d^1$ LS and HS levels for free Tm^{2+} amounts to 1830 cm^{-1}[40] and can be subtracted from the retrieved energy of the $(^3H_6,5d^1)_{S=1/2}$ LS excitation band to determine the location of the Tm^{2+} $(^3H_6,5d^1)_{S=3/2}$ HS excitation band. This latter band should then be positioned at around 15715 cm^{-1} or 635 nm. In the spectra of Figure 4a, it is perceived as a weak band near 630 nm. The inset provides a close-up image of this band. As a result of the rather small crystal field splitting, we were not able to distinguish and identify any additional Tm^{2+} $4f^{12}5d^1$ bands, as these overlap in the range below 500 nm.

3.2.2. Classification of Emissions. When comparing the presented excitation spectra from Figure 4a with the Dieke diagram,[37] it becomes clear that no Tm^{3+} levels are located near the Tm^{2+} $(^3H_6,5d^1)_{S=1/2}$ band at 570 nm or 17545 cm^{-1}. This enables us to selectively excite these Tm^{2+} levels and monitor the Tm^{2+} luminescence.

In Figure 5, the normalized emission spectra are displayed after excitation into the Tm^{2+} $(^3H_6,5d^1)_{S=1/2}$ level. Up to three distinct Tm^{2+} emissions can be observed: two broad and intertwined $4f^{12}5d^1 \rightarrow 4f^{13}$ emissions, positioned close to 735 and 815 nm, and a sharp $4f^{13} \rightarrow 4f^{13}$ line emission near 1140 nm that corresponds to the $^2F_{5/2} \rightarrow {}^2F_{7/2}$ transition. This latter emission has been reported many times before,[16−27] and compared to the other two broad $4f^{12}5d^1 \rightarrow 4f^{13}$ emissions, its intensity in orthorhombic $BaCl_2$ appears to be relatively high at low temperatures.

In the previous study by Grimm et al.,[21] the $4f^{12}5d^1 \rightarrow 4f^{13}$ emissions at 735 and 815 nm were both ascribed to the $(^3H_6,5d^1)_{S=3/2} \rightarrow {}^2F_{7/2}$ transition and explained via the existence of two different species with no further specification of what these might be. In this work, we assign the $4f^{12}5d^1 \rightarrow 4f^{13}$ emission at 735 nm to the spin-allowed (SA) $(^3H_6,5d^1)_{S=1/2} \rightarrow {}^2F_{7/2}$ transition emerging from the LS state and the emission at 815 nm to the spin-forbidden (SF) $(^3H_6,5d^1)_{S=3/2} \rightarrow {}^2F_{7/2}$ transition stemming from the HS state. As such, orthorhombic $BaCl_2$:Tm^{2+} is the very first chloride compound in which the Tm^{2+} spin-allowed $(^3H_6,5d^1)_{S=1/2} \rightarrow {}^2F_{7/2}$ emission is identified. Up to now, it has only been identified in iodide and bromide host lattices: AI_2:Tm^{2+} (A = Ca and Sr), $RbCaI_3$:Tm^{2+}, $CsCaX_3$:Tm^{2+}, and NaX:Tm^{2+} (X = Br and I).[17,19,20,22,24−27] With this classification of emissions, the Tm^{2+} LS Stokes shift in orthorhombic $BaCl_2$ then amounts to 3940 cm^{-1}. Often the Stokes shift in a compound appears to be the same for different lanthanides,[41] and we may compare the Stokes shift for Tm^{2+} with that for Sm^{2+} and Eu^{2+} in orthorhombic $BaCl_2$. From the work of He et al.[29] on orthorhombic $BaCl_2$:Sm^{2+}, the first maximum of the $4f^55d^1$ excitation is observed at around 530 nm or 18870 cm^{-1} and can be attributed to the SmB band. The much weaker SmA $4f^55d^1$ band is then expected to be positioned at about 1855 cm^{-1} lower energy or 585 nm. The work of Lauer and Fong[28] also shows the SmB band at 530 nm with the SmA band hidden in its long wavelength tail. The lowest energy Sm^{2+} $4f^55d^1 \rightarrow 4f^6$ emission is at 660 nm or 15150 cm^{-1},[28] yielding a Stokes shift of 1915 cm^{-1}. For a detailed description on the nomenclature of the SmA and SmB band,[42] the reader is referred to the works of Wood and Kaiser[43] and Yanase.[44]

The work of Brixner and Ferretti[32] on orthorhombic $BaCl_2$:Eu^{2+} provides the lowest energy Eu^{2+} LS $4f^65d^1$ level at around 375 nm and reveals the lowest energy SA $4f^65d^1 \rightarrow 4f^7$ emission at about 405 nm. This yields a Stokes shift of 1915 cm^{-1} that is similar to the value obtained for $BaCl_2$:Sm^{2+}. It now appears that, other than expected, the Stokes shift for Tm^{2+} as a dopant in orthorhombic $BaCl_2$ is more than two times larger than for Sm^{2+} and Eu^{2+}. This indicates that the local coordination of Tm^{2+} in the 5d excited state is different from that of Eu^{2+} and Sm^{2+} due to incorporation on an asymmetric Ba^{2+} site[45,46] with much larger size difference between the dopant ion and the host lattice ion for Tm^{2+} as compared to Eu^{2+} and Sm^{2+}, resulting in a stronger relaxation in the excited 5d state and, consequently, larger Stokes shift.

After the two $4f^{12}5d^1 \rightarrow 4f^{13}$ emissions were deconvolved into separate peaks, an excitation spectrum was made on each of the emissions. These spectra are displayed in Figures 4b,c and show much resemblance in shape to each other and to the spectra acquired on the $^2F_{5/2} \rightarrow {}^2F_{7/2}$ ($4f^{13} \rightarrow 4f^{13}$) emission shown in panel (a). It indicates that the two $4f^{12}5d^1 \rightarrow 4f^{13}$ emissions are definitely related to Tm^{2+} and, moreover, to the same Tm^{2+} center. In addition, the intensity of the two $4f^{12}5d^1 \rightarrow 4f^{13}$ emissions appears to be relatively low at 20 K as compared to the $4f^{13} \rightarrow 4f^{13}$ line emission (see Figure 5). In contrast to other Tm^{2+}-doped halides, the spin-allowed $(^3H_6,5d^1)_{S=1/2} \rightarrow {}^2F_{7/2}$ emission in orthorhombic $BaCl_2$:Tm^{2+} appears to be much stronger than both the $(^3H_6,5d^1)_{S=1/2} \rightarrow {}^2F_{7/2}$ and $(^3H_6,5d^1)_{S=3/2} \rightarrow {}^2F_{7/2}$ emissions[17,19,20,22,24−27] and the spin-forbidden $(^3H_6,5d^1)_{S=3/2} \rightarrow {}^2F_{7/2}$ emission. The very small bump located at around 615 nm cannot be linked to a Tm^{2+} transition and is likely to be related to defect emission or an artifact caused by the sample holder. A summary overview of the different emissions and excitation bands is provided by the scaled-in energy level scheme in Figure 6.

3.2.3. Qualitative Description of Quenching Processes. With the different Tm^{2+} emissions classified in accordance to their transition, the temperature-dependent behavior of these emissions is investigated, and possible quenching mechanisms are explored. Figure 7 shows a plot of the integrated emission intensity of the various Tm^{2+} emissions for temperatures in the range of 20−350 K. The plot is normalized and extrapolated on the measured $^2F_{5/2} \rightarrow {}^2F_{7/2}$ quantum efficiency at 300 K (19%) and based on a deconvolution between the

https://doi.org/10.1021/acs.jpcc.3c04638
J. Phys. Chem. C 2023, 127, 19017−19026

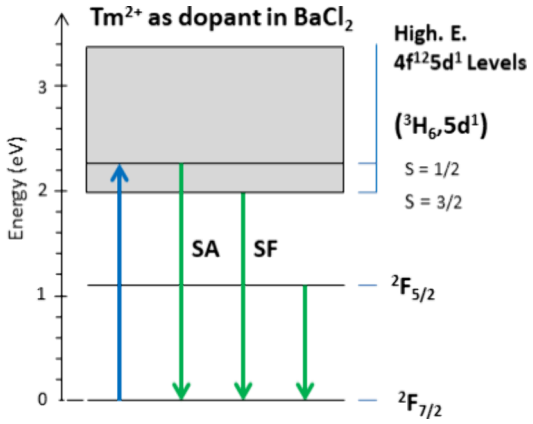

Figure 6. Scaled energy level scheme for Tm^{2+} as a dopant in $BaCl_2$ with an orthorhombic structure. Upon excitation into the low-spin $(^3H_6)_{S=1/2}$ levels (blue arrow) at 20 K, three distinct Tm^{2+} emissions are observed (green arrows). Note: SA = spin-allowed; SF = spin-forbidden.

$(^3H_6,5d^1)_{S=1/2} \rightarrow {}^2F_{7/2}$ and $(^3H_6,5d^1)_{S=3/2} \rightarrow {}^2F_{7/2}$ emissions. In addition, the data are corrected for the sensitivity of detection as described in Section 2.3. As Figure 7 shows, all three Tm^{2+} emissions are present at 20 K, the ${}^2F_{5/2} \rightarrow {}^2F_{7/2}$ ($4f^{13} \rightarrow 4f^{13}$) emission and the $(^3H_6,5d^1)_{S=3/2} \rightarrow {}^2F_{7/2}$ and $(^3H_6,5d^1)_{S=1/2} \rightarrow {}^2F_{7/2}$ ($4f^{12}5d^1 \rightarrow 4f^{13}$) emissions, with estimated quantum efficiencies of, respectively, 18, 1.6, and 2.5%. As the temperature increases, the $(^3H_6,5d^1)_{S=1/2} \rightarrow {}^2F_{7/2}$ and $(^3H_6,5d^1)_{S=3/2} \rightarrow {}^2F_{7/2}$ emissions undergo a rapid quenching, and at around 120 K, both $4f^{12}5d^1 \rightarrow 4f^{13}$ emissions have quenched completely and are no longer observed. Moreover, the inset in Figure 5 reveals that the more intense $(^3H_6,5d^1)_{S=1/2} \rightarrow {}^2F_{7/2}$ emission quenches at an almost equal rate as the weaker $(^3H_6,5d^1)_{S=3/2} \rightarrow {}^2F_{7/2}$ emission. This is reflected in the related T_{50} values, the temperature at which the emissions are at half their initial intensity, which amounts to 53 K for the $(^3H_6,5d^1)_{S=1/2} \rightarrow {}^2F_{7/2}$ emission and 55 K for the $(^3H_6,5d^1)_{S=3/2} \rightarrow {}^2F_{7/2}$ emission. In addition, the Arrhenius thermal deactivation energies, which are provided in Sections 9.1 and 9.2 of the Supporting Information, are very close and respectively amount to 100 and 140 cm^{-1}. Within the temperature range of 20−100 K, the ${}^2F_{5/2} \rightarrow {}^2F_{7/2}$ emission grows and reaches an estimated QE of about 22% at 100 K. This anticorrelated trend between the $4f^{12}5d^1 \rightarrow 4f^{13}$ and $4f^{13} \rightarrow 4f^{13}$ emissions indicates a clear feeding from the $4f^{12}5d^1$ levels to the ${}^2F_{5/2}$ $4f^{13}$ level. As the temperature increases further, the ${}^2F_{5/2} \rightarrow {}^2F_{7/2}$ emission gradually becomes weaker and reaches a QE of about 18% at 350 K.

Based on the excitation spectra presented in Figure 4, the energy gap between the $(^3H_6,5d^1)_{S=1/2}$ and $(^3H_6,5d^1)_{S=3/2}$ levels amounts to 1675 cm^{-1} (see Section 9.3 in the Supporting Information and Table 2). With the maximum phonon energy of 210 cm^{-1}, measured by Lauer and Fong[28] for orthorhombic $BaCl_2$, about 8 phonons are required to bridge this gap. This number is relatively low compared to other Tm^{2+}-doped halides where the $(^3H_6,5d^1)_{S=1/2} \rightarrow {}^2F_{7/2}$ emission in combination with the $(^3H_6,5d^1)_{S=3/2} \rightarrow {}^2F_{7/2}$ emission was observed. In these compounds, the $(^3H_6,5d^1)_{S=1/2} \rightarrow {}^2F_{7/2}$ emission was found to quench via $(^3H_6,5d^1)_{S=1/2} \rightarrow (^3H_6,5d^1)_{S=3/2}$ multiphonon relaxation, and we expect the same for $BaCl_2$:Tm^{2+}. The quenching of the $(^3H_6,5d^1)_{S=1/2} \rightarrow {}^2F_{7/2}$ emission via multiphonon relaxation will feed the $(^3H_6,5d^1)_{S=3/2}$ levels and evoke the $(^3H_6,5d^1)_{S=3/2} \rightarrow {}^2F_{7/2}$ emission. As already mentioned, this latter emission quenches at around the same temperature as the $(^3H_6,5d^1)_{S=1/2} \rightarrow {}^2F_{7/2}$ emission. The energy gap between the $(^3H_6,5d)_{S=3/2}$ and ${}^2F_{5/2}$ levels amounts to 7100 cm^{-1} and corresponds to around 34 phonons, being much larger than the number of phonons required for the $(^3H_6,5d^1)_{S=1/2}-(^3H_6,5d^1)_{S=3/2}$ energy gap.

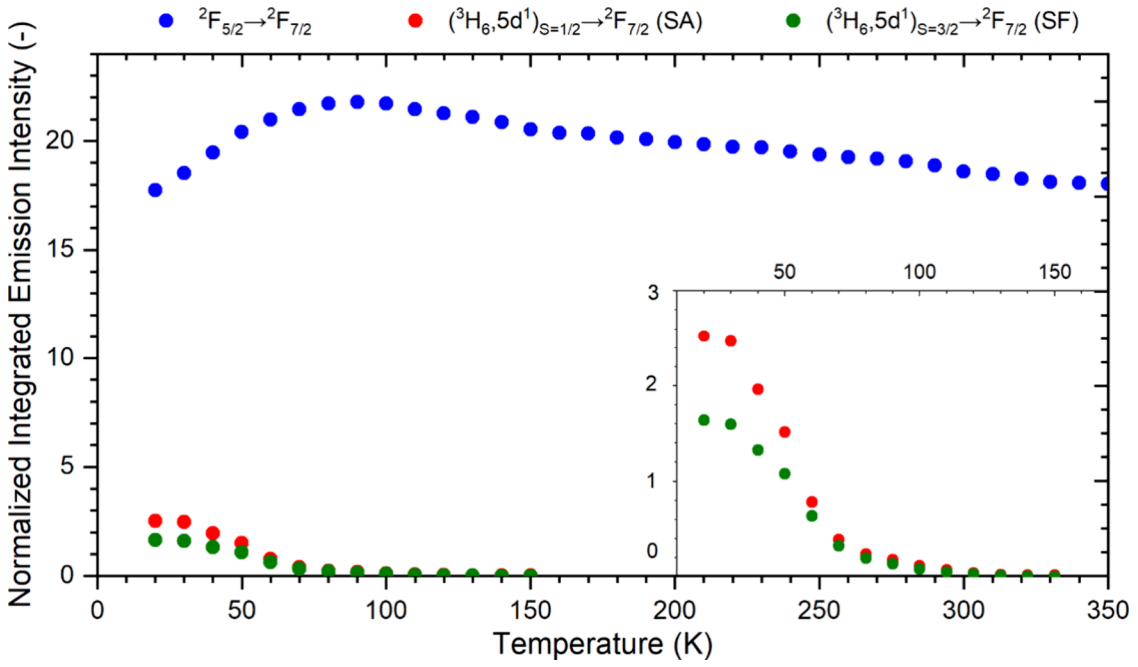

Figure 7. Plot showing the integrated emission intensity of the ${}^2F_{5/2} \rightarrow {}^2F_{7/2}$ (blue), $(^3H_6,5d^1)_{S=1/2} \rightarrow {}^2F_{7/2}$ (red), and $(^3H_6,5d^1)_{S=3/2} \rightarrow {}^2F_{7/2}$ (green) emissions after excitation into the $(^3H_6,5d^1)_{S=1/2}$ levels at 570 nm. The data is normalized and extrapolated on the measured ${}^2F_{5/2} \rightarrow {}^2F_{7/2}$ quantum efficiency at 300 K and corrected for the sensitivity of detection. The inset shows a close-up of the $4f^{12}5d^1 \rightarrow 4f^{13}$ emissions.

https://doi.org/10.1021/acs.jpcc.3c04638
J. Phys. Chem. C 2023, 127, 19017−19026

Table 2. Comparison of Important Quenching Properties for Different Tm^{2+}-Doped Chlorides[a]

material symmetry	energy gap (cm^{-1})[a]	phonon energy (cm^{-1})	req phonons (−)[a]	Stokes shift (cm^{-1})[b]	Stokes shift (cm^{-1})[c]
NaCl:Tm^{2+} O_h	1930[24]	207[49]	10	720[24]	
$CaCl_2$:Tm^{2+} C_{2h}	1735[26]	270[50]	7	1390[26]	
$SrCl_2$:Tm^{2+} O_h	1790[21]	190[51]	10	990[21]	
$BaCl_2$:Tm^{2+} C_S	1675 (this work)	210[28]	8	3600 (this work)	3940 (this work)
$CsCaCl_3$:Tm^{2+} O_h	1720[27]	310[22]	6	830[27]	

[a]Between $(^3H_6,5d^1)_{S=1/2}$–$(^3H_6,5d^1)_{S=3/2}$ levels. [b]$(^3H_6,5d^1)_{S=3/2} \rightarrow {}^2F_{7/2}$ emission. [c]$(^3H_6,5d^1)_{S=1/2} \rightarrow {}^2F_{7/2}$ emission. [d]Of these materials, orthorhombic $BaCl_2$:Tm^{2+} is the only compound in which the $(^3H_6,5d^1)_{S=1/2} \rightarrow {}^2F_{7/2}$ emission is observed. Values for the energy gaps and Stokes shifts are calculated in Table S3 in the Supporting Information, whereas the phonon energies are retrieved from the literature.

Table S6 in the Supporting Information shows that this required number of phonons is similar to $SrCl_2$:Tm^{2+} but larger than for NaCl:Tm^{2+}, $CaCl_2$:Tm^{2+}, and $CsCaCl_3$:Tm^{2+}. Yet, in all of these compounds, the $(^3H_6,5d^1)_{S=3/2} \rightarrow {}^2F_{7/2}$ emission quenches at a much higher temperature than observed for orthorhombic $BaCl_2$:Tm^{2+}. For instance, for $CaCl_2$:Tm^{2+}, the $(^3H_6,5d^1)_{S=3/2} \rightarrow {}^2F_{7/2}$ emission starts to quench at 20 K and is no longer observed at 260 K, having quenched completely.[21] The $(^3H_6,5d^1)_{S=3/2} \rightarrow {}^2F_{7/2}$ emission in orthorhombic $BaCl_2$:Tm^{2+} quenching solely via multiphonon relaxation, as was suggested by Grimm et al.,[21] thus seems unlikely.

In our recent study on CaX_2:Tm^{2+} (X = Cl, Br, and I),[26] we found that the $(^3H_6,5d^1)_{S=3/2} \rightarrow {}^2F_{7/2}$ emission also undergoes thermal quenching via interband crossing. This $4f^{12}5d^1 \rightarrow 4f^{13}$ quenching process involves the crossing point between the $(^3H_6,5d^1)_{S=3/2}$ and $^2F_{5/2}$ state parabolas, as illustrated in Figure 8.[26,27,47,48] The energy of the crossing point will be situated at a relatively low energy in the case of a small energy gap between the $(^3H_6,5d^1)_{S=3/2}$ and $^2F_{5/2}$ levels and/or a large value for the Stokes shift of the $(^3H_6,5d^1)_{S=3/2} \rightarrow {}^2F_{7/2}$ emission,

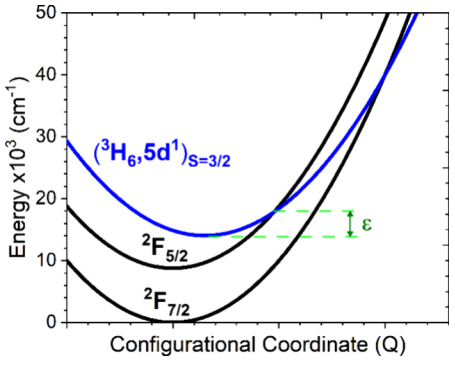

Figure 8. Configurational coordinate diagram revealing the $Tm^{2+}{}^2F_{7/2}$, $^2F_{5/2}$, and $(^3H_6,5d^1)_{S=3/2}$ state parabolas. The crossing point between the $(^3H_6,5d^1)_{S=3/2}$ and $^2F_{5/2}$ states exemplifies the quenching process of interband crossing, which is activated at a specific temperature when enough thermal energy ε is available for reaching the crossing point. At an even higher temperature, the crossing point between the $(^3H_6,5d^1)_{S=3/2}$ and $^2F_{7/2}$ ground state will be thermally provoked.[26,27,47,48]

giving rise to efficient quenching via interband crossing. For orthorhombic $BaCl_2$:Tm^{2+}, the related energy gap amounts to 7100 cm^{-1} and is around 1.5 times larger than in $CaBr_2$:Tm^{2+}, where it amounts to 4745 cm^{-1}.[26] However, the related Stokes shift in orthorhombic $BaCl_2$:Tm^{2+} is 3600 cm^{-1} (see Table 2) and almost 3 times larger than for $CaBr_2$:Tm^{2+},[26] where it amounts to only 1245 cm^{-1}. So, the relatively low quenching temperature of the $(^3H_6,5d^1)_{S=3/2} \rightarrow {}^2F_{7/2}$ emission can be a consequence of the large Stokes shift. Furthermore, as the Stokes shift of the $(^3H_6,5d^1)_{S=1/2} \rightarrow {}^2F_{7/2}$ emission is of almost similar size to that of the $(^3H_6,5d^1)_{S=3/2} \rightarrow {}^2F_{7/2}$ emission, the former emission might also undergo quenching via $(^3H_6,5d^1)_{S=1/2} \rightarrow {}^2F_{5/2}$ interband crossing in addition to $(^3H_6,5d^1)_{S=1/2} \rightarrow (^3H_6,5d^1)_{S=3/2}$ multiphonon relaxation.

As the $(^3H_6,5d^1)_{S=1/2} \rightarrow {}^2F_{7/2}$ and $(^3H_6,5d^1)_{S=3/2} \rightarrow {}^2F_{7/2}$ emissions undergo thermal quenching, the $^2F_{5/2}$ level becomes populated, resulting in $^2F_{5/2} \rightarrow {}^2F_{7/2}$ emission. Figure 7 shows that above 100 K, the $^2F_{5/2} \rightarrow {}^2F_{7/2}$ emission becomes weaker. The energy gap between the $^2F_{5/2}$ and $^2F_{7/2}$ $4f^{13}$ levels is around 8770 cm^{-1}, corresponding with 42 phonons, and is therefore too large for efficient multiphonon relaxation to take place at the relatively low temperature of 100 K. Yet, the intensity decrease in the $^2F_{5/2} \rightarrow {}^2F_{7/2}$ emission intensity could be related to interband crossing between the $(^3H_6,5d^1)_{S=3/2}$ levels and the $^2F_{7/2}$ ground state. This process is generally triggered at very high temperatures.[45,46,20] However, the exceptionally large $4f^{12}5d^1$ Stokes shift for Tm^{2+} as a dopant in orthorhombic $BaCl_2$ makes it likely for such a process to occur at much lower temperatures. $(^3H_6,5d^1)_{S=3/2} \rightarrow {}^2F_{7/2}$ interband crossing would offer an efficient nonradiative quenching route from the $(^3H_6,5d^1)_{S=3/2}$ levels directly to the $^2F_{7/2}$ ground state, bypassing the $^2F_{5/2}$ level and thereby omitting the $^2F_{5/2} \rightarrow {}^2F_{7/2}$ emission. The presence of such a nonradiative route at 100 K would explain not only why the $^2F_{5/2} \rightarrow {}^2F_{7/2}$ emission intensity becomes weaker above this temperature but also why its QE is nonunity at room temperature.

3.2.4. Presence of SA $(^3H_6,5d^1)_{S=1/2} \rightarrow {}^2F_{7/2}$ Emission. Orthorhombic $BaCl_2$:Tm^{2+} is the very first chloride compound in which the Tm^{2+} spin-allowed $(^3H_6,5d^1)_{S=1/2} \rightarrow {}^2F_{7/2}$ emission is assigned. Up to now, it has only been reported in iodide and bromide host lattices: AI_2:Tm^{2+} (A = Ca and Sr), $RbCaI_3$:Tm^{2+}, $CsCaX_3$:Tm^{2+}, and NaX:Tm^{2+} (X = Br and I).[17,19,20,22,24−27] In contrast to other Tm^{2+}-doped halides that display both the $(^3H_6,5d^1)_{S=1/2} \rightarrow {}^2F_{7/2}$ and $(^3H_6,5d^1)_{S=3/2} \rightarrow {}^2F_{7/2}$ emissions,[17,19,20,22,24−27] the spin-allowed $(^3H_6,5d^1)_{S=1/2} \rightarrow {}^2F_{7/2}$ emission in orthorhombic $BaCl_2$:Tm^{2+} also appears to be much stronger than the spin-forbidden $(^3H_6,5d^1)_{S=3/2} \rightarrow {}^2F_{7/2}$ emission.

In the works of de Jong et al.[39,40] on $CsCaX_3$:Tm^{2+} (X = Cl and Br), it was revealed that for small energy gaps between the $(^3H_6,5d^1)_{S=3/2}$ and $(^3H_6,5d^1)_{S=1/2}$ levels, corresponding to 5 or fewer phonons, there will be a rapid relaxation to the $(^3H_6,5d^1)_{S=3/2}$ level, and no Tm^{2+} $(^3H_6,5d^1)_{S=1/2} \rightarrow {}^2F_{7/2}$ luminescence is to be expected. However, as Table 2 shows, the respective energy gap for orthorhombic $BaCl_2$:Tm^{2+} is of almost a similar size to that of other Tm^{2+}-doped chlorides. Therefore, the spontaneous presence of the $(^3H_6,5d^1)_{S=1/2} \rightarrow {}^2F_{7/2}$ emission in orthorhombic $BaCl_2$:Tm^{2+} seems unrelated to a relatively slower quenching via multiphonon relaxation.

However, our study on the temperature-dependent relaxation dynamics of CaX_2:Tm^{2+} (X = Cl, Br, and I)[26]

https://doi.org/10.1021/acs.jpcc.3c04638
J. Phys. Chem. C 2023, 127, 19017−19026

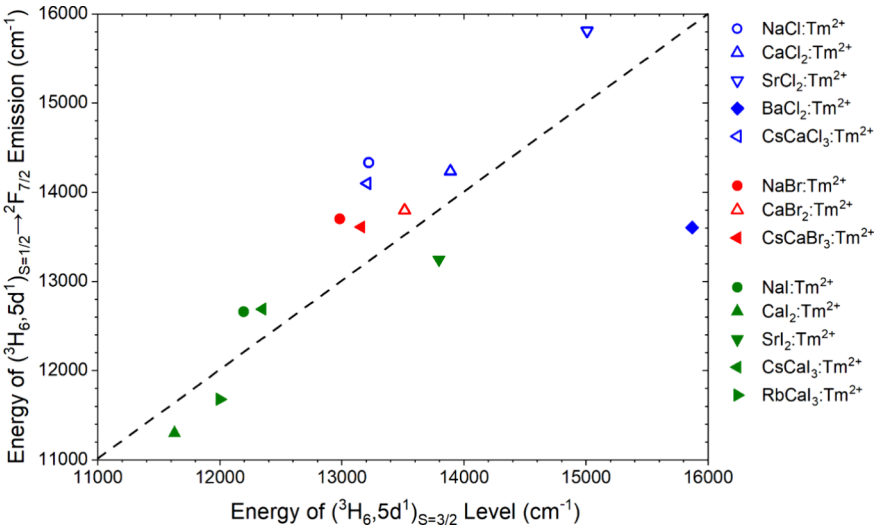

Figure 9. Graph showing the absorption energy of the $(^3H_6,5d^1)_{S=3/2}$ levels plotted versus the luminescence energy of the $(^3H_6,5d^1)_{S=1/2} \rightarrow {}^2F_{7/2}$ emission for all previously studied Tm^{2+}-doped halides, excluding fluorides.[19,21,24−27] The closed symbols represent compounds in which the $(^3H_6,5d^1)_{S=1/2} \rightarrow {}^2F_{7/2}$ emission was perceived, while for the open symbols, this emission was not observed, but its presumed energy was calculated from the $4f^{12}5d^1$ Stokes shift. The $(^3H_6,5d^1)_{S=1/2} \rightarrow {}^2F_{7/2}$ emission has a relatively strong luminescence signature in compounds, where its energy is lower than the $(^3H_6,5d^1)_{S=3/2}$ absorption energy. Note that the line serves as an aid to the eye.

revealed that for $CaCl_2:Tm^{2+}$ and $CaBr_2:Tm^{2+}$, the energy of the $(^3H_6,5d^1)_{S=1/2} \rightarrow {}^2F_{7/2}$ emission matched quite well with the absorption energy of the $(^3H_6,5d^1)_{S=3/2}$ levels. The absence of $(^3H_6,5d^1)_{S=1/2} \rightarrow {}^2F_{7/2}$ emission in these compounds is therefore ascribed by us to a $(^3H_6,5d^1)_{S=1/2} \rightarrow (^3H_6,5d^1)_{S=3/2}$ energy transfer process. During this process, the $(^3H_6,5d^1)_{S=1/2} \rightarrow {}^2F_{7/2}$ luminescence is absorbed by a neighboring Tm^{2+} ion, leading to ${}^2F_{7/2} \rightarrow (^3H_6,5d^1)_{S=3/2}$ excitation. To provide stronger evidence for the possible absence of such a process in orthorhombic $BaCl_2:Tm^{2+}$, we decided to evaluate the data of all known Tm^{2+}-doped halides. Figure 9 shows the luminescence energy of the $(^3H_6,5d^1)_{S=1/2} \rightarrow {}^2F_{7/2}$ emission as plotted versus the absorption energy of the $(^3H_6,5d^1)_{S=3/2}$ levels; values are found in Table S7 in the Supporting Information. In this figure, data from Tm^{2+}-doped chlorides are provided in blue, whereas that related to bromides is shown in red and that of iodides is shown in green. The closed symbols represent compounds in which the $(^3H_6,5d^1)_{S=1/2} \rightarrow {}^2F_{7/2}$ emission has been observed, while the open symbols portray those in which it is absent. For this latter category, the presumed energy of the $(^3H_6,5d^1)_{S=1/2} \rightarrow {}^2F_{7/2}$ emission was calculated by subtracting the $4f^{12}5d^1$ Stokes shift of the $(^3H_6,5d^1)_{S=3/2} \rightarrow {}^2F_{7/2}$ emission from the energy of the $(^3H_6,5d^1)_{S=1/2}$ absorption band. As Figure 9 shows for orthorhombic $BaCl_2:Tm^{2+}$, the energy of the $(^3H_6,5d^1)_{S=1/2} \rightarrow {}^2F_{7/2}$ emission is far lower than the absorption energy of the $(^3H_6,5d^1)_{S=3/2}$ levels. This means that the energy transfer process from the $(^3H_6,5d^1)_{S=1/2}$ state to the $(^3H_6,5d^1)_{S=3/2}$ state cannot take place, and consequently, a strong $(^3H_6,5d^1)_{S=1/2} \rightarrow {}^2F_{7/2}$ emission is observed. In the case of $SrI_2:Tm^{2+}$,[25] $CaI_2:Tm^{2+}$,[26] and $RbCaI_3:Tm^{2+}$,[19] the energy of the $(^3H_6,5d^1)_{S=1/2} \rightarrow {}^2F_{7/2}$ emission is also, but somewhat, lower than the absorption energy of the $(^3H_6,5d^1)_{S=3/2}$ levels and we observe a relatively strong $(^3H_6,5d^1)_{S=1/2} \rightarrow {}^2F_{7/2}$ emission. For the other Tm^{2+}-doped halides in Figure 9, the energy of the $(^3H_6,5d^1)_{S=1/2} \rightarrow {}^2F_{7/2}$ emission is higher than the absorption energy of the $(^3H_6,5d^1)_{S=3/2}$ levels, resulting in a high probability of $(^3H_6,5d^1)_{S=1/2} \rightarrow (^3H_6,5d^1)_{S=3/2}$ energy transfer, and hence, the $(^3H_6,5d^1)_{S=1/2} \rightarrow {}^2F_{7/2}$ emission is either very weak or not observed at all. For all discussed materials, there will also be $(^3H_6,5d^1)_{S=1/2} \rightarrow (^3H_6,5d^1)_{S=3/2}$ multiphonon relaxation. For chlorides, the required amounts of phonons are relatively small as compared to bromides and iodides (see Table S5 in the Supporting Information). This will lead to efficient multiphonon relaxation, on top of the energy transfer process, and causes the $(^3H_6,5d^1)_{S=1/2} \rightarrow {}^2F_{7/2}$ emission to be absent.[17,20,21,24,26,27]

4. CONCLUSIONS

As compared to other Tm^{2+}-doped halides, the luminescence properties of $BaCl_2:Tm^{2+}$ with an orthorhombic structure are quite special and somewhat deviating. At 20 K, the well-known ${}^2F_{5/2} \rightarrow {}^2F_{7/2}$ ($4f^{13} \rightarrow 4f^{13}$) line emission and two $4f^{12}5d^1 \rightarrow 4f^{13}$ band emissions are observed, which can be attributed to the spin-allowed $(^3H_6,5d^1)_{S=1/2} \rightarrow {}^2F_{7/2}$ and spin-forbidden $(^3H_6,5d^1)_{S=3/2} \rightarrow {}^2F_{7/2}$ transition. However, orthorhombic $BaCl_2:Tm^{2+}$ is the first chloride compound where the Tm^{2+} spin-allowed $(^3H_6,5d^1)_{S=1/2} \rightarrow {}^2F_{7/2}$ emission is observed. Previously, it has only been seen in Tm^{2+}-doped iodides and a selective group of bromides with low phonon energies. Its presence observed for orthorhombic $BaCl_2:Tm^{2+}$ is explained by the absence of a $(^3H_6,5d^1)_{S=1/2} \rightarrow (^3H_6,5d^1)_{S=3/2}$ energy transfer process that causes the $(^3H_6,5d^1)_{S=1/2} \rightarrow {}^2F_{7/2}$ emission to be absorbed by the $(^3H_6,5d^1)_{S=3/2}$ levels of a neighboring Tm^{2+} ion. As the temperature increases, the $(^3H_6,5d^1)_{S=1/2} \rightarrow {}^2F_{7/2}$ emission undergoes thermal quenching via $(^3H_6,5d^1)_{S=1/2} \rightarrow (^3H_6,5d^1)_{S=3/2}$ multiphonon relaxation and is no longer observed at 120 K, having quenched completely. In the same temperature range of 20−120 K, the $(^3H_6,5d^1)_{S=3/2} \rightarrow {}^2F_{7/2}$ emission also undergoes thermal quenching. Due to the exceptionally large $4f^{12}5d^1$ Stokes shift, this emission most likely quenches via $(^3H_6,5d^1)_{S=3/2} \rightarrow {}^2F_{5/2}$ interband crossing. As both $4f^{12}5d^1 \rightarrow 4f^{13}$ emissions quench, a direct feeding route toward the ${}^2F_{5/2}$ level emerges and the ${}^2F_{5/2} \rightarrow {}^2F_{7/2}$ ($4f^{13} \rightarrow 4f^{13}$) emission increases in intensity. Above 100 K, however, the intensity of this emission starts to decrease unexpectedly. We suspect that this decrease

https://doi.org/10.1021/acs.jpcc.3c04638
J. Phys. Chem. C 2023, 127, 19017−19026

is related to interband crossing between the $(^3H_6,5d^1)_{S=3/2}$ levels and the $^2F_{7/2}$ ground state, resulting in the QE of the $^2F_{5/2} \rightarrow {}^2F_{7/2}$ emission to be nonunity at room temperature.

■ ASSOCIATED CONTENT

Supporting Information

The Supporting Information is available free of charge at https://pubs.acs.org/doi/10.1021/acs.jpcc.3c04638.

Arrhenius plot and thermal deactivation energy of the $(^3H_6,5d^1)_{S=1/2} \rightarrow {}^2F_{7/2}$ emission, Arrhenius plot and thermal deactivation energy of the $(^3H_6,5d^1)_{S=3/2} \rightarrow {}^2F_{7/2}$ emission, quantification of luminescence and quenching properties for different Tm^{2+}-doped halides, and quantification of luminescence properties regarding the presence of the SA $(^3H_6,5d^1)_{S=1/2} \rightarrow {}^2F_{7/2}$ emission in different Tm^{2+}-doped halides (PDF)

■ AUTHOR INFORMATION

Corresponding Author

Maarten P. Plokker − *Faculty of Applied Sciences, Dept. Radiation Science and Technology, Delft University of Technology, 2629 JB Delft, The Netherlands;* orcid.org/0000-0002-1939-0649; Email: maartenplokker@hotmail.com

Authors

Sophie Vlaar − *Faculty of Applied Sciences, Dept. Radiation Science and Technology, Delft University of Technology, 2629 JB Delft, The Netherlands*

Aaron H. J. Bakx − *Faculty of Applied Sciences, Dept. Radiation Science and Technology, Delft University of Technology, 2629 JB Delft, The Netherlands*

Erik van der Kolk − *Faculty of Applied Sciences, Dept. Radiation Science and Technology, Delft University of Technology, 2629 JB Delft, The Netherlands*

Pieter Dorenbos − *Faculty of Applied Sciences, Dept. Radiation Science and Technology, Delft University of Technology, 2629 JB Delft, The Netherlands*

Hubertus T. Hintzen − *Faculty of Applied Sciences, Dept. Radiation Science and Technology, Delft University of Technology, 2629 JB Delft, The Netherlands*

Complete contact information is available at: https://pubs.acs.org/10.1021/acs.jpcc.3c04638

Notes

The authors declare no competing financial interest.

■ ACKNOWLEDGMENTS

This research was financially supported by the Department of Radiation Science & Technology at Delft University of Technology (TU Delft). The authors would like to thank J. T. M. de Haas for the overall experimental support with the luminescence measurements, B. E. Terpstra for the overall assistance with ICP-OES measurement, and N. Dusoswa for helping out with the fluorescence quantum yield measurement.

■ REFERENCES

(1) Kiss, Z. J. Energy levels of divalent thulium in CaF_2. *Phys. Rev.* **1962**, *127* (3), 718−724.

(2) McClure, D. S.; Kiss, Z. Survey of the spectra of the divalent rare-earth ions in cubic crystals. *J. Chem. Phys.* **1963**, *39* (12), 3251−3257.

(3) Duncan, R. C., Jr.; Kiss, Z. J. Continuously operating CaF_2:Tm^{2+} optical Maser. *Appl. Phys. Lett.* **1963**, *3* (2), 23−24.

(4) Kiss, Z. J.; Pressley, R. J. Crystalline solid lasers. *Appl. Opt.* **1966**, *5* (10), 1474−1486.

(5) Stockbarger, D. C. The production of large single crystals of lithium fluoride. *Rev. Sci. Instrum.* **1936**, *7*, 133−136.

(6) Hayes, W.; Jones, G. D.; Twidell, J. W. Paramagnetic resonance and optical absorption of irradiated CaF_2:Ho. *Proc. Phys. Soc.* **1963**, *81*, 371−373.

(7) *RCA Laboratories quarterly status reports*; No. *4*, Wright-Patterson Ohio (USA), April (1962).

(8) Schipper, W. J.; Meijerink, A.; Blasse, G. The luminescence of Tm^{2+} in strontium tetraborate. *J. Lumin.* **1994**, *62*, 55−59.

(9) Solarz, P.; Komar, J.; Głowacki, M.; Berkowski, M.; Ryba-Romanowski, W. Spectroscopic characterization of SrB_4O_7:Tm^{2+}, a potential laser material and optical temperature sensor. *RSC Adv.* **2017**, *7*, 21085−21092.

(10) Zheng, T.; Sójka, M.; Runowski, M.; Woźny, P.; Lis, S.; Zych, E. Tm^{2+} Activated SrB_4O_7 Bifunctional Sensor of Temperature and Pressure—Highly Sensitive, Multi-Parameter Luminescence thermometry and Manometry. *Adv. Opt. Mater.* **2021**, *9* (22), 34546−34551.

(11) Sinha, S. P. *Systematics and the properties of the lanthanides, P.3−16 author W*; ASI Series C, Reidel Publishing: Klemm, NATO, ISBN-978−94−009−7175−2; 1982.

(12) Meyer, G. Reduced halides of the rare-earth elements. *Chem. Rev.* **1988**, *88*, 93−107.

(13) Rubio, J. O. Doubly-valent rare-earth ions in halide crystals. *J. Phys. Chem.* **1991**, *52* (1), 101−174.

(14) Wickleder, C. Spectroscopic properties of $SrZnCl_4$:M^{2+} and $BaZnCl_4$:M^{2+} (M = Eu, Sm, Tm). *J. Alloys Compd.* **2000**, *300−301*, 193−198.

(15) Wenger, O. S.; Wickleder, C.; Krämer, K. W.; Güdel, H. U. upconversion in a divalent rare earth ion: optical absorption and luminescence spectroscopy of Tm^{2+} doped $SrCl_2$. *J. Lumin.* **2001**, *94−95*, 101−105.

(16) Grimm, J.; Beurer, E.; Güdel, H. U. Crystal absorption spectra in the region of 4f-4f and 4f-5d excitations in Tm^{2+}-doped $CsCaCl_3$, $CsCaBr_3$, and $CsCaI_3$. *Inorg. Chem.* **2006**, *45*, 10905−10908.

(17) Grimm, J.; Güdel, H. U. Five different types of spontaneous emission simultaneously observed in Tm^{2+} doped $CsCaBr_3$. *Chem. Phys. Lett.* **2005**, *404*, 40−43.

(18) Beurer, E.; Grimm, J.; Gerner, P.; Güdel, H. U. New type of near-infrared to visible photon upconversion in Tm^{2+}-doped $CsCaI_3$. *J. Am. Chem. Soc.* **2006**, *128*, 3110−3111.

(19) Beurer, E.; Grimm, J.; Gerner, P.; Güdel, H. U. Absorption, light emission, and upconversion properties of Tm^{2+}-doped $CsCaI_3$ and $RbCaI_3$. *Inorg. Chem.* **2006**, *45*, 9901−9906.

(20) Grimm, J.; Suyver, J. F.; Beurer, E.; Carver, G.; Güdel, H. U. Light-emission and excited-state dynamics in Tm^{2+} doped $CsCaCl_3$, $CsCaBr_3$, and $CsCaI_3$. *J. Phys. Chem. B* **2006**, *110*, 2093−2101.

(21) Grimm, J.; Wenger, O.S.; Krämer, K. W.; Güdel, H. U. 4f−4f and 4f−5d excited states and luminescence properties of Tm^{2+}-doped CaF_2, $CaCl_2$, $SrCl_2$ and $BaCl_2$. *J. Lumin.* **2007**, *126*, 590−596.

(22) Grimm, J.; Beurer, E.; Gerner, P.; Güdel, H. U. upconversion between 4f−5d excited states in Tm^{2+}-doped $CsCaCl_3$, $CsCaBr_3$, and $CsCaI_3$. *Eur. J. Chem.* **2007**, *13*, 1152−1157.

(23) ten Kate, O. M.; Krämer, K. W.; Van der Kolk, E. Efficient luminescent solar concentrators based on self-absorption free Tm^{2+} doped halides. *Sol. Energy Mater. Sol. Cells* **2015**, *140*, 115−120.

(24) Plokker, M. P.; van der Kolk, E. Temperature dependent relaxation dynamics of luminescent NaX:Tm^{2+} (X = Cl, Br, I). *J. Lumin.* **2019**, *216*, 116694.

(25) Plokker, M. P.; Hoogsteen, W.; Abellon, R. D.; Krämer, K. W.; van der Kolk, E. Concentration and temperature dependent luminescence properties of the SrI_2-TmI_2 system. *J. Lumin.* **2020**, *225*, 117327.

(26) Plokker, M. P.; van der Knijff, I. C.; de Wit, A. V.; Voet, B.; Woudstra, T.; Khanin, V.; Dorenbos, P.; van der Kolk, E.

Experimental and numerical analysis of Tm^{2+} excited-states dynamics and luminescence in CaX_2 (X = Cl, Br, I). *J. Phys.: Condens. Matter* **2021**, *33* (25), 255701.
(27) Plokker, M. P.; Biner, D. A.; Dusoswa, N.; Dorenbos, P.; Krämer, K. W.; van der Kolk, E. Photoluminescence and excited states dynamics of Tm^{2+}-doped $CsCa(Cl/Br)_3$ and $CsCa(Br/I)_3$ perovskites. *J. Phys. Mater.* **2021**, *4* (4), No. 045004.
(28) Lauer, H. V., Jr.; Fong, F. K. Role of the $4f^5 5d$ band in the radiationless $^5D_1 \rightarrow {}^5D_0$ coupling in $BaCl_2:Sm^{2+}$ and $BaBr_2:Sm^{2+}$. *J. Chem. Phys.* **1976**, *65* (8), 3108−3117.
(29) He, Z.; Wang, Y.; Li, S.; Xu, X. Dynamic studies on the time-resolved fluorescence of Sm^{2+} in $BaCl_2$. *J. Lumin.* **2002**, *97*, 102−106.
(30) Dixie, L. C.; Edgar, A.; Reid, M. F. Sm^{2+} fluorescence and absorption in cubic $BaCl_2$: Strong thermal crossover of fluorescence between $4f^6$ and $4f^5 5d^1$ configurations. *J. Lumin.* **2012**, *132*, 2775−2782.
(31) Rogers, E.; Dorenbos, P.; de Haas, J. T. M.; van der Kolk, E. Experimental study of the $4f^n \rightarrow 4f^n$ and $4f^n \rightarrow 4f^{n-1}5d^1$ transitions of the lanthanide diiodides LnI_2 (Ln = Nd, Sm, Eu, Dy, Tm, Yb). *J. Phys.: Condens. Matter* **2012**, *24* (27), No. 275502.
(32) Brixner, L. H.; Ferretti, A. Eu^{2+} Fluorescence in $BaCl_2$. *J. Solid State Chem.* **1976**, *18*, 111−116.
(33) Edgar, A.; Bartle, M.; Varoy, C.; Raymond, S.; Williams, G. Structure and Scintillation Properties of Cerium-Doped Barium Chloride Ceramics: Effects of Cation and Anion Substitution. *IEEE Trans. Nucl. Sci.* **2010**, *57* (3), 1218−1222.
(34) Edgar, A.; Zimmermann, J.; von Seggern, H.; Varoy, C.R. Lanthanum-stabilized europium-doped cubic barium chloride: An efficient x-ray phosphor. *Int. J. Appl. Phys.* **2010**, *107*, 083516.
(35) Ting, V. P.; Henry, P. F.; Schmidtmann, M.; Wilson, C. C.; Weller, M. T. Probing hydrogen positions in hydrous compounds: information from parametric neutron powder diffraction studies. *Phys. Chem. Chem. Phys.* **2012**, *14* (19), 6914−6921.
(36) Shannon, R. D. Revised Effective Ionic Radii and Systematic Studies of Interatomic Distances in Halides and Chalcogenides. *Acta Crystallogr., Sect. A: Cryst. Phys., Diffr., Theor. Gen. Crystallogr.* **1976**, *32*, 751−767.
(37) Dieke, G. H.; Crosswhite, H. M. The Spectra of the Doubly and Triply Ionized Rare Earths. *Appl. Opt.* **1963**, *2* (7), 675−686.
(38) Dorenbos, P. Crystal field splitting of lanthanide $4f^{n-1}5d$-levels in inorganic compounds. *J. Alloys Compd.* **2002**, *341* (1−2), 156−159.
(39) de Jong, M.; Biner, D.; Krämer, K. W.; Barandiarán, Z.; Seijo, L.; Meijerink, A. New insights in $4f^{12}5d^1$ excited states of Tm^{2+} through excited state excitation spectroscopy. *J. Phys. Chem. Lett.* **2016**, *7* (14), 2730−2734.
(40) de Jong, M.; Meijerink, A.; Seijo, L.; Barandiaran, Z. Energy level structure and multiple $4f^{12}5d^1$ emission bands for Tm^{2+} in halide perovskites: theory and experiment. *J. Phys. Chem. C* **2017**, *121* (18), 10095−10101.
(41) Dorenbos, P. Energy of the first $4f^7 \rightarrow 4f^6 5d$ transition of Eu^{2+} in inorganic compounds. *J. Lumin.* **2003**, *104* (4), 239−260.
(42) Dorenbos, P. f→d transition energies of divalent lanthanides in inorganic compounds. *J. Phys.: Condens. Matter* **2003**, *15* (3), 575−594.
(43) Wood, D. L.; Kaiser, W. Absorption and Fluorescence of Sm^{2+} in CaF_2, SrF_2 and BaF_2. *Phys. Rev.* **1962**, *126* (6), 2079−2088.
(44) Yanase, A. Optical Absorption of Sm^{2+} in CaF_2 Type Crystals. *J. Phys. Soc. Jpn.* **1977**, *42* (5), 1680−1686.
(45) Daicho, H.; Shinomiya, Y.; Enomoto, K.; Nakano, A.; Sawa, H.; Matsuishi, S.; Hosonoc, H. A novel red-emitting $K_2Ca(PO_4)F:Eu^{2+}$ phosphor with a large Stokes shift. *Chem. Commun.* **2018**, *54* (8), 884−887.
(46) Bagatur'yants, A. A.; Iskandarova, I. M.; Knizhnik, A. A.; Mironov, V. S.; Potapkin, B. V.; Srivastava, A. M.; Sommerer, T. J. Energy level structure of 4f5d states and the Stokes shift in $LaPO_4:Pr^{3+}$: A theoretical study. *Phys. Rev. B* **2008**, *78* (16), 165125.
(47) Struck, C. W.; Fonger, W. H. *Understanding Luminescence Spectra and Efficiency Using Wp and Related Functions, Inorganic Chemistry Concepts 13*; Springer Verlag ISBN 3−540−52766−4; 1991.
(48) Grinberg, M.; Lesniewski, T. Non-radiative processes and luminescence quenching in Mn^{4+} doped phosphors. *J. Lumin.* **2019**, *214*, 116574.
(49) Burstein, E.; Johnson, F. A.; Loudon, R. Selection Rules for Second-Order Infrared and Raman Processes in the Rocksalt Structure and Interpretation of the Raman Spectra of NaCl, KBr, and NaI. *Phys. Rev.* **1965**, *139* (4A), A1239.
(50) Karbowiak, M.; Maciejewska, K.; Rudowicz, C. Trends in Hamiltonian parameters determined by systematic analysis of f-d absorption spectra of divalent lanthanides in alkalihalides hosts: II. $CaCl_2:Ln^{2+}$ (Ln = Sm, Eu, Tm, and Yb). *J. Lumin.* **2019**, *215*, 116622.
(51) Schreyer, D.; Waschk, V.; Châtelain, A. Raman spectroscopy in small crystals of $SrCl_2$. *Surf. Sci.* **1981**, *106* (1−3), 336−344.

https://doi.org/10.1021/acs.jpcc.3c04638
J. Phys. Chem. C 2023, 127, 19017−19026